


Nonlinear amplification of nano bowl surface concavity on the critical response threshold to biosignals

Received: 20 February 2024

Xuefeng Li¹, Xin Liang¹, Cuiqin Yang^{1,2} & Qiang Yan^{1,2} 

Accepted: 30 September 2024

Published online: 08 October 2024

 Check for updates

Polymer nanoparticles that can sharply sense and detect biological signals in cells are promising candidates for biomedical and theranostic nanomaterials. However, the response ability of current polymer assemblies poorly matches the requirement of trace concentration level (10^{-6} - 10^{-9} mol/L) of cellular biosignals due to their linear signal input-to-function output mode, which impedes their practical applications in vivo. Here we report a kind of nanobowl system with pH-tunable invaginated morphology that can nonlinearly amplify the response abilities toward biosignals by modulating the surface concavity. Compared to conventional spherical nanoparticles, nonspherical nanobowls with a specific concave structure reduce the critical response threshold of polymers by up to 5 orders of magnitude, from millimole to nanomole level, covering most of biosignal concentration windows. Moreover, we find that this nonlinear signal gain effect is originated from the collective impact of a single signal on transitioning the polymer chain aggregation state of individual assemblies, rather than just altering a certain unit or chain. This nonlinear signal-to-response mechanism is potential to solve the tricky problems of probing and sensing endogenous signals with trace physiological concentration.

Biological signaling molecules are acknowledged as the major regulators for message transfer of living organisms owing to their pivotal role in cell communications^{1,2}. They mediate almost all cellular response events, including signal transduction, metabolic regulation, oxidative stress, and immune processes³⁻⁵. Normally, signaling molecules produced endogenously can maintain homeostasis to meet essential requirements of cell activities; nevertheless, once this balance is broken, even subtle fluctuations in their concentrations will cause severe diseases^{6,7}. As such, this feature makes biosignals a class of hallmarks to differentiate pathological abnormalities from physiological states, a major challenge in any diagnostic and therapeutic applications^{8,9}. Based on this principle, the past decade has witnessed extensive advances in stimuli-responsive polymer engineering that capitalizes on biosignals as the main cues because of their promising prospects in bio-imaging, drug delivery, and clinical theranostics¹⁰⁻¹².

Compared with other common external stimuli, one of the most conspicuous characteristics of biosignals is their trace level in the cell milieu, typically on the order of micromolar–nanomolar range (10^{-6} - 10^{-9} mol/L)^{13,14}. This requires that responsive polymers themselves must possess extremely low critical response thresholds (C_T), so as to sharply sense and probe the minute variations of biosignal concentration in vivo. Presently, most known polymers basically follow a one-to-one (1-to-1) response mode, that is, one molecule of signal input can only trigger the output of one responsive unit, usually reflected by the cleavage of that unit from polymer (Fig. 1a)^{15,16}. In this context, to realize complete functional expression it necessitates biosignals with the same stoichiometry to responsive units in the polymer. This results in relatively high C_T values (10^{-3} - 10^{-4} mol/L) that far exceed their level in cells^{17,18}. To fulfill the goal of lowering C_T , another effective way is to employ a self-immolative polymer,

¹State Key Laboratory of Molecular Engineering of Polymers, Fudan University, No.220, Handan Road, Shanghai, China. ²Department of Macromolecular Science, Fudan University, No.2005, Songhu Road, Shanghai, China. ✉e-mail: yanq@fudan.edu.cn

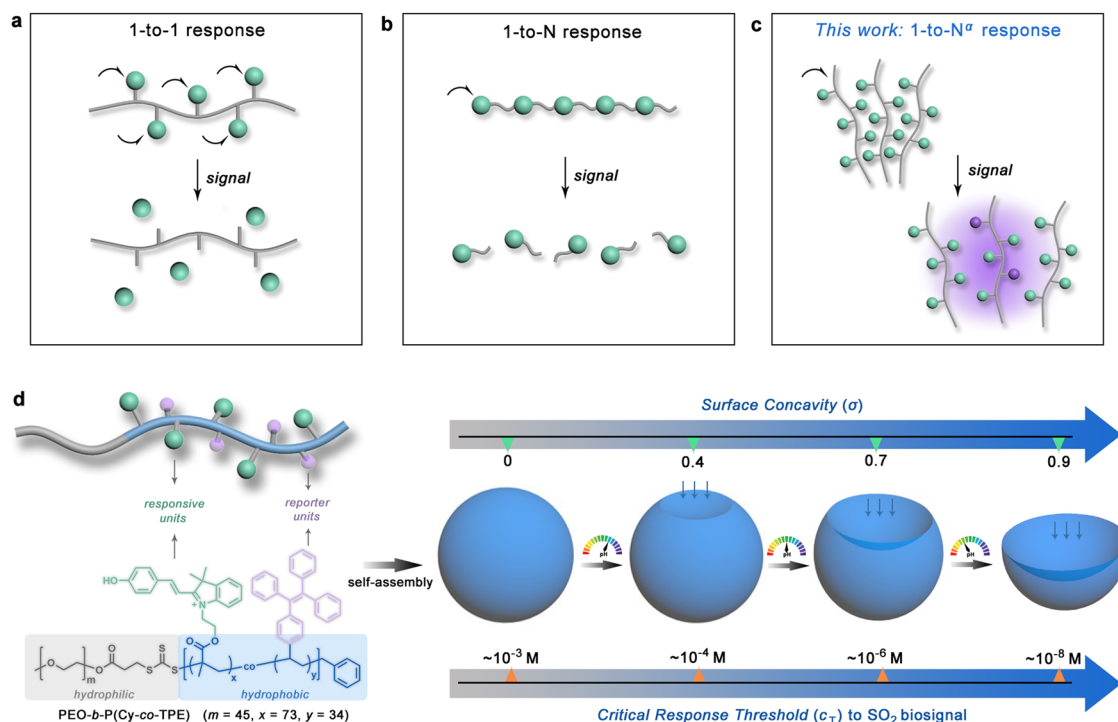


Fig. 1 | Illustration of traditional signal-to-response modes and the design concept of signal nonlinear amplification by regulation of surface concavity of nano bowls. **a** '1-to-1' response mode by side-group-type responsive polymers. **b** '1-to-N' response mode by main-chain-type self-immolative polymers. **c** This work

presents a '1-to- N^α ' response mode by chain aggregation state mutation. **d** Designed SO_2 -biosignal-responsive block copolymer, PEO-*b*-P(Cy-co-TPE), and its self-assembly shape transformation with a pH-tunable surface concavity that confers to the nonlinear amplifying effect of response-ability towards SO_2 biosignal.

a main-chain-type macromolecule that can dissociate from head to tail through a domino-like fragmentation when its head group is reacted with a biosignal¹⁹. This method allows linear amplification of a single signal by a factor of N ('1-to- N ', N is the number of immolative nodes, Fig. 1b)^{20,21}. In spite of this, there still remains a certain gap between C_T and actual biosignal level due to the finite N value, which may affect the practical biological applications of related materials²².

To overcome this insurmountable obstacle, the quest for an efficient response mode capable of nonlinear amplification between signal input and functional output is a possible solution. Here, we report a bowl-like polymer assembled system with variable depressed morphology that manifests an unprecedented exponential growth in response-ability to biosignal by tuning the surface concavity. Such nano bowls are assembled from cyanine-containing amphiphilic block copolymers, where common poly (ethylene oxide) (PEO) serves as the hydrophilic chain while polycyanine (PCy) is introduced as the responsive segment. In our recent work, PCy has been shown to sense a type of gas signaling molecule, sulfur dioxide (SO_2), which is endogenous and involved in the regulation of physiological and pathological functions in numerous organs^{23–25}, and be converted into a negatively charged indole species via nucleophilic addition of C=C double bond with bisulfate²⁶. In addition, tetraphenylethylene-based monomers (TPE) were also copolymerized on the blockchain as the fluorescent reporters to quantify this responding output through its aggregation-induced emission (AIE) effect^{27,28}. Such copolymers (denoted as PEO-*b*-P(Cy-co-TPE)) tend to pre-form large complex spherical structures (LCS) because of their small volume ratio of hydrophilic PEO segment ($f_{\text{PEO}} \sim 7\%$)²⁹. The addition of SO_2 gas would induce the conversion of hydrophobic, conjugated Cy groups into charged, non-conjugated indole (Ino) forms, thus evoking a detectable fluorescent decline through changing the aggregation state of TPEs. Not surprisingly, this response defers to a linear correlation with SO_2 concentration, like other biosignal-responsive

polymeric systems^{17,18,30–32}. This leaves the C_T range merely on the order of $\sim 10^{-3}$ mol/L, failing to match the intracellular SO_2 concentration of 10^{-8} – 10^{-9} mol/L³³. Yet, an unexpected discovery is that these LCSs are quite plastic in morphology, like rubbery balls, whose outer shell could undergo a local invagination with fine pH regulation, gradually deforming into a kind of non-canonical bowl-shaped nanostructure. Spectral variations of the assembled solution provide molecular-level evidence of this deformation process, demonstrating that hydrogen-bonding interactions between the hydroxyl groups on the Cy motifs and π - π stacking between the conjugated structures combine to facilitate the morphology transition from balls to bowls. Moreover, as the degree of surface collapse is deepening ($0 \rightarrow 1$), the response-ability of concave nano bowls toward SO_2 as compared to the initial nanospheres would exponentially jump by 5 orders of magnitude (C_T , $10^{-3} \rightarrow 10^{-8}$ mol/L), as shown in Fig. 1d, which is anticipated to significantly enhance the value of the materials for applications in real biological environments and assist in enhancing the specific biodistribution of the specific drugs in the SO_2 lesion cells. We conjecture, that the collective impact of a single signal on shifting the chain aggregation state inside an individual assembly, rather than just response to a certain unit or chain, might be the reason for this nonlinear signal gain (Fig. 1c). This is a meaningful attempt to explore the relationship between the block copolymer self-assembly morphology and their stimulus response ability. We envision that this present strategy has the potential to apply to other broad-spectrum biological signals, which will provide us guidance on nanoparticle shape selection for in situ detection of various pathophysiological hallmarks in trace levels.

Results

Design of SO_2 -biosignal-responsive polymers

Aiming to achieve the above design rationale, a Cy compound possessing a peculiar phenol group was chosen as the SO_2 -sensitive

monomer. The installation of phenolic hydroxyl functionality makes it susceptible to external pH³⁴. In a weak alkaline environment, the deprotonated phenol anions could produce slight repulsion with each other, but in an acidic solution, they could be reversible protonation and form intermolecular H-bonding, which will become a driving force to regulate the nano bowl geometry. On the other hand, vinyl tetraphenylethylene (TPE) was prepared as the self-reporting monomer. Not only could it express the degree of interchain aggregation via the shift in emission intensity, but it also assists the polymer-assembled transition by participation in the π - π stacking of the hydrophobic core of the assemblies, which enhances π - π interactions^{27,35}. The monomers were well-characterized by ¹H and ¹³C NMR and mass spectrometer (Supplementary Figs. 1–4). With these two functional monomers, reversible addition-fragmentation chain transfer (RAFT) polymerizations using trithioester-capped PEO as macromolecular chain transfer agent afforded a series of diblock copolymers with varying comonomer compositions, including PEO₄₅-*b*-P(Cy₇₃-*co*-TPE₃₄), PEO₄₅-*b*-P(Cy₇₈-*co*-TPE₉), and PEO₄₅-*b*-P(Cy₂₈-*co*-TPE₃₀). Their respective structures were confirmed by ¹H NMR and GPC analysis (Supplementary Figs. 20–22), and the compositional parameters were summarized in Supplementary Table 1.

As a control, we also synthesized three kinds of block copolymer counterparts. First, PEO₄₅-*b*-PCy₇₀ and PEO₄₅-*b*-PTPE₅₈, paucity of the fluorophores and responsive pendants, respectively, were prepared to show that the cooperative effect of Cy and TPE units is a prerequisite for the fabrication of nano bowls. Second, C₃TPE and C₁₁TPE monomers with short and long aliphatic spacers were adopted instead of TPE to afford copolymers, PEO₄₅-*b*-P(Cy₆₉-*co*-C₃TPE₃₂) and PEO₄₅-*b*-P(Cy₇₃-*co*-C₁₁TPE₃₄). Since the flexible alkyl chains impeded the stacking interactions among TPEs, neither of their assemblies had enough inward depression in-depth, which can function as polymer contrasts to reveal the role of surface concavity on the amplifying signal. Third, using pyrene (Py), a fluorophore with aggregation-caused quenching (ACQ) effect to replace TPE³⁶, obtained PEO₄₅-*b*-P(Cy₇₅-*co*-Py₃₂) copolymer as counterpart for comparing the difference of response-ability with TPE-bearing ones. The aforesaid monomers were structurally verified (Supplementary Figs. 5–19), and all the polymerizations were of high conversion (>80%) and relatively narrow distribution (\bar{D} = 1.1–1.2, Supplementary Figs. 23–28 and Table 2).

With the as-designed Cy-containing polymer series in hand, we first surveyed their specific reactivity to SO₂ by ¹H NMR analysis. Taking PEO₄₅-*b*-P(Cy₇₃-*co*-TPE₃₄) as a representative, prior to gas stimulus, it gave a diagnostic proton peak at δ = 6.26 ppm (H_A), assigned to the free double bond in Cy pendants. However, after purging with SO₂ (2 mM, equal molar amount to that of Cy units in polymer), this peak completely vanished while a new broad signal at δ = 9.30 ppm corresponding to the sulfonate proton (H_B) appeared simultaneously (Fig. 2a). This means that SO₂ can react with the Cy side groups in polymer chain via nucleophilic addition, structurally converting into sulfonate-substituted polyindole (PIno)^{26,37}. A depressed absorption around 530 nm ascribed to Cy chromophore probed by UV-Vis spectroscopy corroborated this point (Supplementary Fig. 31). Notably, this process is reversible. Peroxides (e.g., H₂O₂) can facilitate the elimination of the bisulfate group via oxidation, which induces an inversion from Ino to Cy species and thus restores the polymer structural form (Supplementary Fig. 32). On the other hand, we also cared about this response selectivity of copolymers, because in addition to SO₂ biosignal, there coexisted many endogenous interfering substances in the cell. Not only are their reactivity analogous to SO₂, but most of them also have higher physiological levels. Using a palette of nucleophilic anions (Cl⁻, Br⁻, I⁻, S₂O₃²⁻, NO₃⁻, HPO₄²⁻, and HCO₃⁻) and gas signaling molecules (NO, N₂O, NH₃, CO, and H₂S) as analytes to treat with our copolymer, the resulted spectral variations were all negligible ($\Delta A/A_0$ < 5%), indicating its excellent anti-interference and specific recognition to SO₂ in intricate cell milieu (Fig. 2b and Supplementary Fig. 33).

Polymer self-assembly behavior and nano bowl formation

After ensuring that the polymer has good SO₂ reactivity, we wanted to explore their self-assembly behavior in solution. Owing to the amphiphilicity, PEO₄₅-*b*-P(Cy₇₃-*co*-TPE₃₄) can spontaneously form aggregates by the common selective solvent method³⁸. To eliminate the influence of polymer concentration and cosolvent ratio on the assemblies, it was dissolved in THF, followed by slowly addition of H₂O precipitant to guarantee the final solution at a constant concentration of 1.0 mg/mL (THF/H₂O, 1/1, v/v). Preliminary studies by transmission electron microscope (TEM) found that the co-polymers in the weak basic milieu (phosphate buffer, pH = 8.3) can organize into typical globular nanostructure (Fig. 2c), and exhibited a nearly uniform size of 510 ± 28 nm by TEM particulate statistics (Supplementary Fig. 34a), consistent with their hydrodynamic diameter of 526 nm and low polydispersity (PDI) of 0.052 measured by dynamic light scattering (Supplementary Fig. 35). Close inspection using scanning electron microscope (SEM) and atomic force microscope (AFM) disclosed that these spheres own solid-like interior and intact, smooth enclosures without holes or cracks on the surface (Fig. 2d, e), indicating that they should belong to typical LCS morphology³⁹. However, as the solution pH dropped below 6.0, they unexpectedly transformed into a kind of non-spherical invaginated aggregates, each possessing a wide open mouth on the surface and one deep cavity inside, and thus we refer to them as nano bowls (NB) (Fig. 2f)^{40,41}. Their mean size remained at 522 ± 35 nm (Supplementary Figs. 34–35), close to that of the original spheres, which implies that such a sphere-to-bowl transition is probably derived from the deformation of assembly individuals as if each nanosphere was subjected to press inwardly to cause a local collapse (arrows in Fig. 2f). SEM and AFM images also supported the formation of nano bowls, as evidenced by the sunken cavitory bodies with sharp contrast to the shell edges (Fig. 2g, h). These results together prove that the geometry of polymer assemblies is of dynamic plasticity, and subtle pH fluctuation can highly concave the surface of the nano bowls. In addition, regardless of nanospheres or nano bowls, they were quite stable in the absence of stimuli, and no obvious size and shape changes were seen for over two months (Supplementary Fig. 36). This indicates that the structure exhibits excellent physical stability, which can be attributed to the high glass transition temperatures of the two motifs that comprise the hydrophobic block in the copolymer (Supplementary Figs. 37, 38).

Tunable surface concavity of nano bowls

What is curious is how solution pH dictates the deformation of NBs and whether their dented degree can be modulated. To elucidate this point, cryogenic TEM (cryo-TEM), high-contrast TEM, and AFM were employed to track the shape evolution of polymer assemblies, in which representative TEM images were selected to analyze the electron-beam intensity profile for evaluating the geometric parameters of NBs. When pH was at 8.3, cryo-TEM revealed that the true form of LCSs in solution was indeed spherically symmetric with a solid-like interior (Fig. 3a, i, ii), and their average diameter (D) was determined to be 523 nm (Fig. 3a, iii, iv). With pH reducing to near neutral (7.6), individual shallow pits emerged on the shell surface, resembling dimpled aggregates (Fig. 3b, i, ii). If we defined the width of the open mouth as W and the vertical depth from the bottom to the top of the pit as H , the two parameters were respectively measured to be 282 ± 29 nm and 164 ± 22 nm from the electron contrast curves (Fig. 3b, iii, iv). This shallow depression nanostructure, termed s-NB, was also confirmed by tapping mode AFM height image, as indicated by the small area of shadow void located in each assembly (Fig. 3b, v). Of further interest was the depressed space could be gradually deepened and extended as the pH decreases (Fig. 3c, i, ii). Upon pH down to 6.8, a more negative concave curvature was obtained, where the H value presented a double elevation to 325 ± 34 nm while W expanded to an average of 336 ± 35 nm (Fig. 3c, iii, iv). AFM also validated the formation of the moderately depressed region on the nano bowl surface (termed as m-NB; Fig. 3c, v).

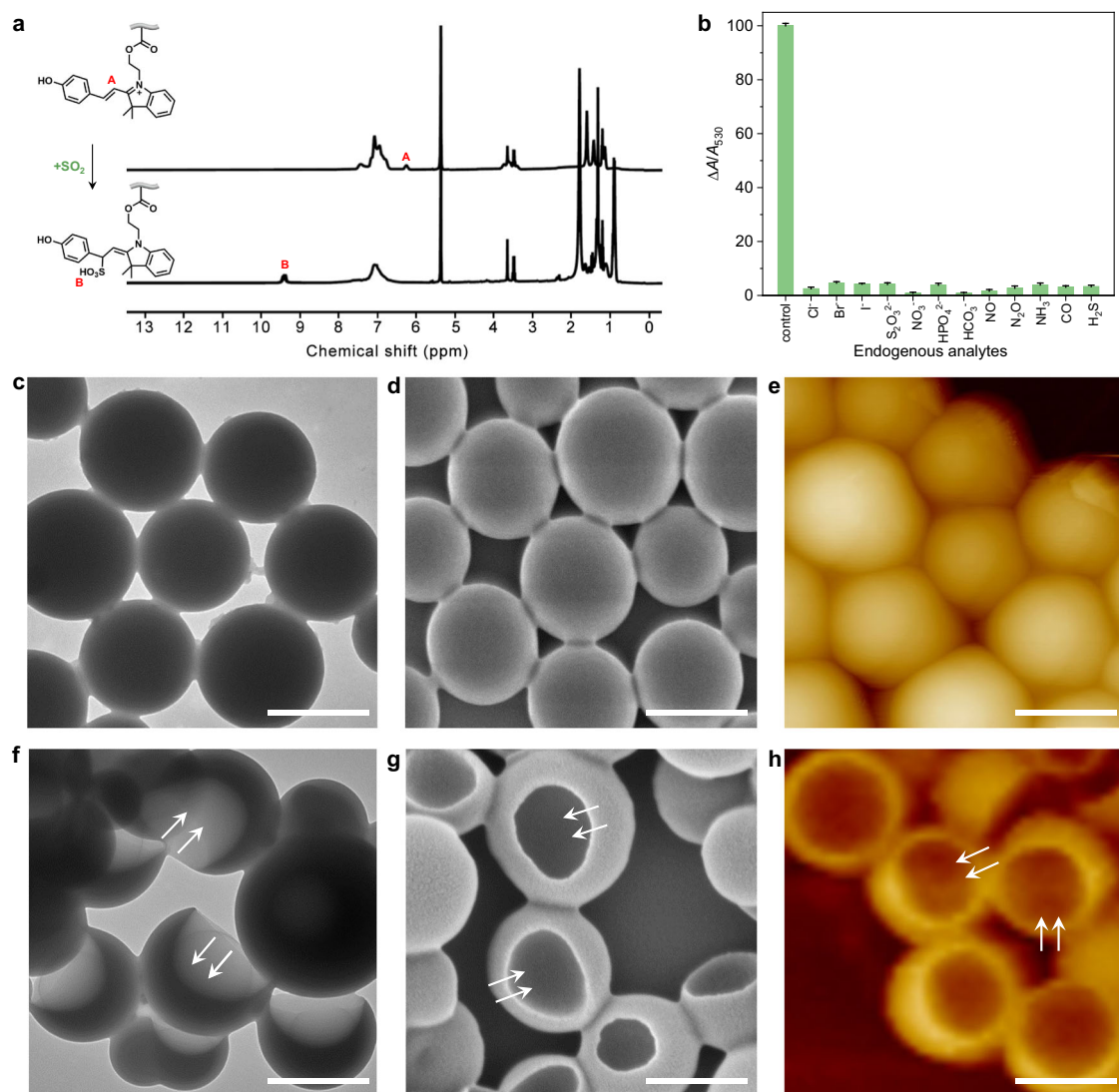


Fig. 2 | Block copolymers responsive to SO₂ and self-assembly transition. **a** ¹H NMR spectra probing the structural change of PEO₄₅-*b*-P(Cy₇₃-*co*-TPE₃₄) in the absence and presence of SO₂. **b** Specific differentiation of PEO₄₅-*b*-P(Cy₇₃-*co*-TPE₃₄) copolymer to SO₂ biosignal from other endogenous analytes. The error bars

indicate the standard deviation ($n = 3$). **c, f** TEM, **(d, g)** SEM, **(e, h)** AFM images of the self-assembly morphologies of PEO₄₅-*b*-P(Cy₇₃-*co*-TPE₃₄) in weak alkaline buffer (pH = 8.3, c-e) and weakly acidic solution (pH = 5.5, f-h). Scale bar: 500 nm.

Eventually, the depth of the depression can attain four-fifths of the nano bowl dimension ($H = 398 \pm 37$ nm), and the opening width can account for 85% of the overall size ($W = 449 \pm 40$ nm) at pH 5.5 (termed as d-NB; Fig. 3d, i-v). In addition to directly regulating the pH of the assembly solution by adjusting the pH of the PBS buffer, we have also attempted an in situ approach to pH regulation, i.e., by incorporating gluconolactone (GL) into the self-assembly solution as an in situ slow acid generator, which can be gradually hydrolyzed to gluconolactone (Supplementary Fig. 39)⁴²⁻⁴⁴. It was found that the evolution of the obtained assembly morphology was similar to the above results (Supplementary Fig. 40), demonstrating that the formation of the bowl-like morphology is not affected by way of pH regulation, which allows it to be free from external control, hinting the broader applications in organisms with abundant physiological pH gradients⁴⁵.

From these results, it can be drawn that the nano bowl concaving degree is well regulated by the pH circumstance. Both W and H , two key geometric factors to describe nano bowl curvature, have a positive correlation with the decrease in pH value (Fig. 4a, blue and green curves). This agrees well with the cross-sectional height analysis by AFM (Fig. 3a-d, vi). But two particular phenomena need to be noted,

one is that the mean radius of NBs is nearly unchanged regardless of how their internal cavities deform (Fig. 4a, gray curve; Supplementary Fig. 41), and the other is that there exists a pH window of NB formation (pH 5.5 - 8.3) and no significant changes occur out of the boundaries (Supplementary Fig. 42). Here, we introduced a geometric scale, surface concavity (σ), to quantitatively represent the extent of inward bending of NBs, where σ is the ratio between the total height of the invagination body and the NB diameter, given by a simple equation (Eq. 1, calculation in Supplementary Fig. 43). By plotting σ data as a function of pH, it results from a near sigmoid-type curve (Fig. 4b). This nonlinear growth presages that the response-ability of NB assemblies may have desired morphology-related nonlinearity.

$$\sigma = \frac{H + R - \sqrt{R^2 - W^2/4}}{2R} \quad (1)$$

In comparison, we also studied other Cy-containing copolymers of different comonomer ratios. For the cases of PEO₄₅-*b*-P(Cy₇₈-*co*-TPE₉) and PEO₄₅-*b*-P(Cy₅₄-*co*-TPE₅) with lower comonomer ratios (0.12

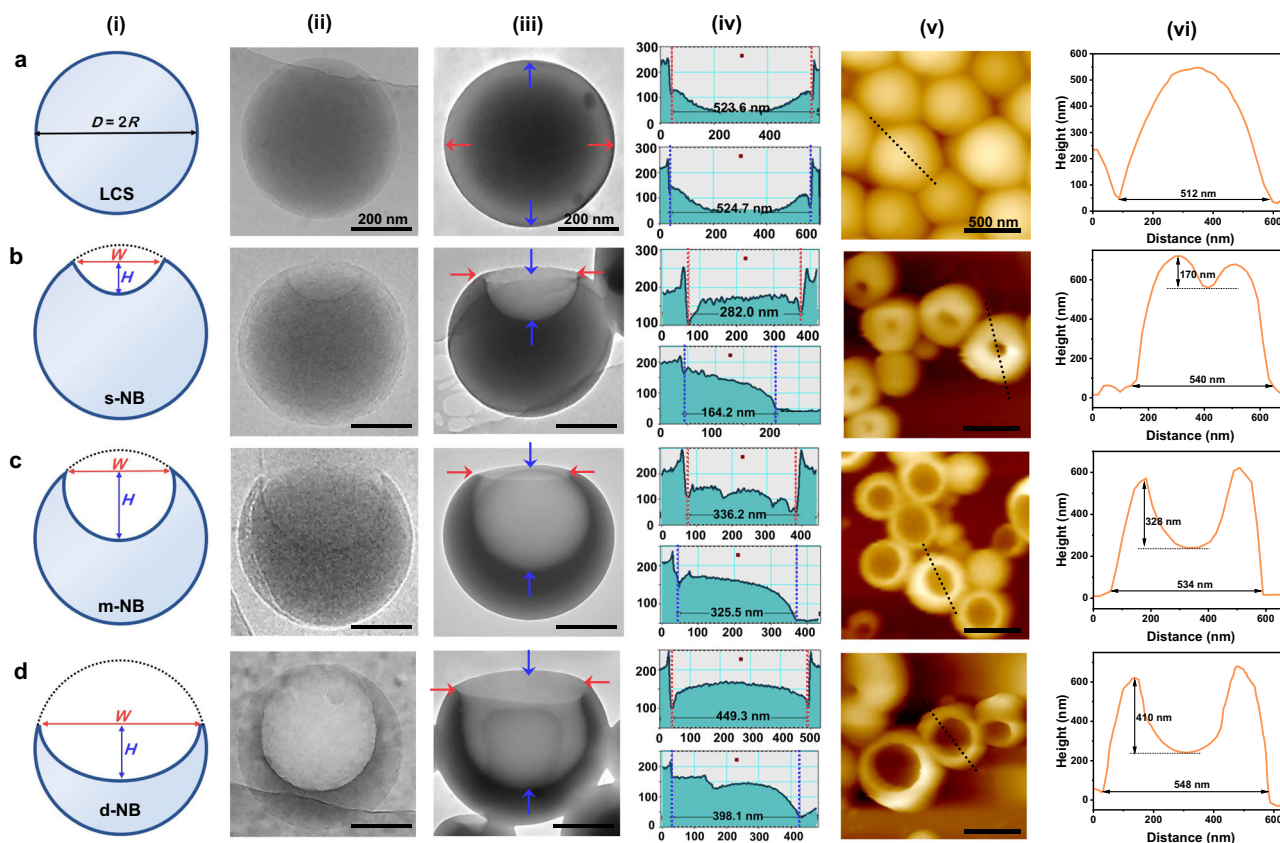


Fig. 3 | Morphological evolution of nano bowls with variable surface concavity. Using different analysis and characterization methods, including (i) geometric illustration of surface invaginated structures, (ii) cryo-TEM, (iii) high-contrast TEM, (iv) electron-beam intensity profile analysis to individual assemblies, (v) tapping-mode AFM height images, and (vi) cross-sectional height analysis, to show the

shape transformation of $\text{PEO}_{45}\text{-}b\text{-P}(\text{Cy}_{73}\text{-}co\text{-TPE}_{34})$ assemblies under various pH conditions. **a** LCSs (pH = 8.3). **b** s-NBs (pH = 7.6). **c** m-NBs (pH = 6.8). **d** d-NBs (pH = 5.5). All the polymer concentrations were at 1.0 mg/mL. The scale bar in series (ii) and (iii) is 200 nm, and in series (v) is 500 nm.

and 0.09, respectively), it was found that the former was unable to form large inward incurvation ($H = 169 \pm 30$ nm, $H/D = 0.34$, Supplementary Fig. 44) since the number of Cy groups in per chain is roughly constant whereas the amount of TPE units decreases three quarters. Further reduction of the comonomer ratio to 0.09, i.e., $\text{PEO}_{45}\text{-}b\text{-P}(\text{Cy}_{54}\text{-}co\text{-TPE}_5)$, resulted in formation of shallower incurvation ($H = 50 \pm 8$ nm, $H/D = 0.18$, Supplementary Fig. 45). In contrast, for the cases of $\text{PEO}_{45}\text{-}b\text{-P}(\text{Cy}_{28}\text{-}co\text{-TPE}_{30})$ and $\text{PEO}_{45}\text{-}b\text{-P}(\text{Cy}_{26}\text{-}co\text{-TPE}_{56})$ with higher comonomer ratios (1.07 and 2.17, respectively), both were found to form d-NBs with deep cavities, with H/D ratios as high as 0.75 and 0.83 (Supplementary Figs. 46, 47). The outcomes of the self-assembly of the five groups of polymers with varying TPE/Cy ratios are presented in Supplementary Table 3 and illustrated in Supplementary Fig. 48, where the variation curves of H/D with TPE/Cy are plotted. It can be observed that as the ratio of TPE/Cy increases, the formation of the distinctive d-NBs becomes more facile. This evidence substantiates the pivotal role of the TPE moiety in driving the formation of d-NBs architecture.

The said facts demonstrate that pH is key to governing the surface geometry of NBs. We postulated that the mechanism is related to the supramolecular synergy among polymer chains, especially possible H-bonding interactions. To figure out this point, infrared (IR) spectroscopic detection of diverse nano bowl shapes were proceeded. As shown in Fig. 4c, LCSs only gave a weak H-bonding vibration at 3426 cm^{-1} . Given that the pK_a of the phenol groups on the polymer can be measured to be ~ 6.56 (Supplementary Fig. 49), it can be concluded that the weak hydrogen bonding interaction is a consequence of the majority of the phenol groups in Cy moieties being deprotonated in the weakly alkaline environment of pH = 8.3, only resulting in weak

interchain interaction. However, with pH decreasing, a reversible protonation brought about a substantial shift of this band to low wavenumber (3350 cm^{-1}) with strengthening, which points to the interchain H-bonding between the interchain $\text{-OH}\cdots\text{HO-}$ ⁴⁶ and thus an enhancement of the interchain cohesion. As the pH is lowered below 5, the protonation of the phenol groups reaches its end, resulting in a halt to the continued increase in interchain hydrogen bonding, which is in accordance with the previous section, where the structure and size of the aggregates remain unchanged when the pH is lowered from 5.5 to 5.0 (Supplementary Fig. 42). In addition to H-bonding effect, their spectrometric properties were also probed. As compared to the soluble unimer, the absorption of initial LCS assemblies exhibited a blue shift from 532 nm to 525 nm (Fig. 4d, gray and light green curves). This means that as long as the copolymers begin to self-organize, the conjugated Cy groups can form H-aggregate via interchain π -stacking, thus leading to a hypochromatic effect⁴⁷. Moreover, the higher extent the nano bowls incurve, the larger shift the spectrum has (Fig. 4d, light green to dark green, $\Delta\lambda = 30$ nm), indicating that the enhancement of interchain H-bonding interactions leads to the gradual aggregation of the chains, which in turn simultaneously enhances the interchain π -stacking by enlarging the area of the π - π interacting domains (as shown in Supplementary Fig. 50). In order to ascertain whether the TPE moiety is involved in the aforementioned process, the UV-vis absorption spectra of the self-assembled solution of $\text{PEO}_{45}\text{-}b\text{-PCy}_{70}$ devoid of PTPE segments were investigated when the pH was decreased. It was found that the blue shift decreased to 18 nm, which is reduced by more than one-third (Supplementary Fig. 52, purple to green), and the self-assembled

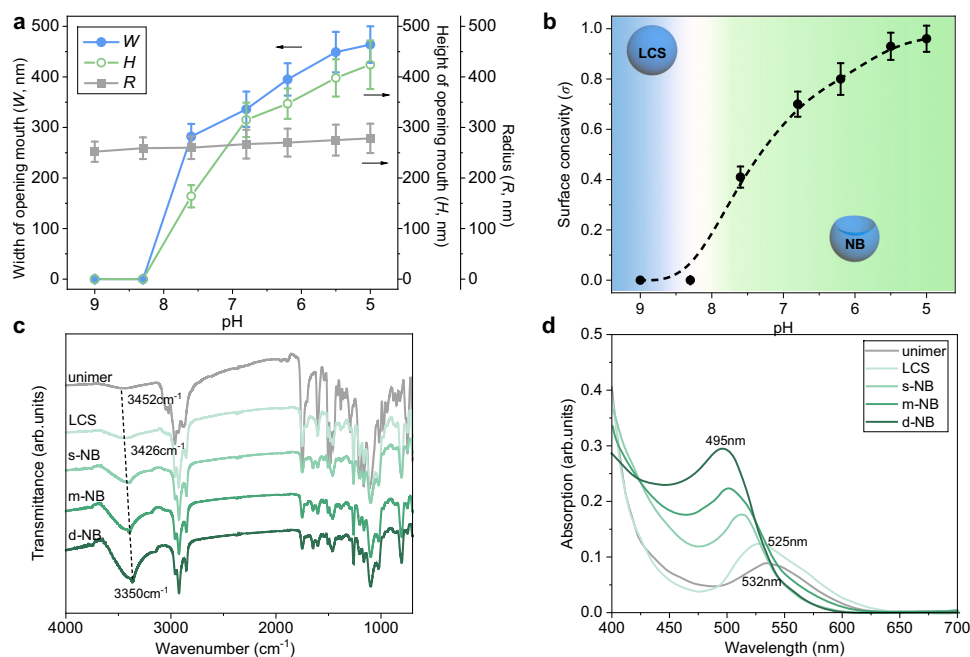


Fig. 4 | Geometric parameter change and spectrometric monitoring of diverse nano bowl shapes. **a** The width (W) and height (H) of open mouth in assemblies and their radius (R) plotted against solution pH. **b** The variation of surface concavity (σ) of the assemblies as a function of solution pH. The border between the two

colors represents the pH point (~ 8.0) at which the LCSs transform into the NBs. Error bars in (**a**, **b**) represent mean \pm s.d., with $n = 3$ independent experiments. **c** Infrared and **d** UV-Vis spectral changes monitoring the supramolecular interactions inside the polymer assemblies with various shapes.

polymer morphology remained spherical (Supplementary Fig. 53), which further substantiates the hypothesis that the TPE moiety can facilitate the formation of NBs by participating in supramolecular interactions within the assemblies. Furthermore, if using PEO₄₅-*b*-PTPE₅₈ without PCy segment, it also failed to assemble into NB due to the absence of π - π interactions between the conjugated Cy groups (Supplementary Fig. 54). The results presented above collectively demonstrate that the Cy and TPE motifs are collectively involved in the aggregation of the hydrophobic core, ultimately leading to a morphological transformation process driven by enhanced interchain interactions⁴⁸.

On the other hand, we found that TPE groups also have an auxiliary effect on NB formation. It seems that only TPE tightly attached to the main chain can act on the nano bowl invagination. On the contrary, the isolation of TPE from the main chain, for example, using PEO₄₅-*b*-P(Cy₆₉-*co*-C₃TPE₃₂) and PEO₄₅-*b*-P(Cy₇₃-*co*-C₁₁TPE₃₄) with spacers, is against the surface concaving (Supplementary Fig. 55). A possible reason is that TPes positioned near the polymer skeleton is rigid whose aggregation intensifies the cohesive forces inside the core, whereas TPE pendants with flexible linkers hinder this effect.

Furthermore, it is important to consider the influence of external forces on morphological transformation, in addition to the supramolecular interaction forces within the assemblies. Among the existing studies, osmotic pressure-induced deformation is one of the more studied approaches. This approach has now successfully helped researchers to obtain a large variety of particles with unique morphologies, including tubular polymersomes⁴⁹, disc⁵⁰, stomatocytes⁵¹, stomatocyte in stomatocyte⁵², and a series of higher-order morphologies with programmable compartment networks⁵³. In order to discuss the guiding role of osmotic pressure in driving the deformation process from balls to bowls, we have also performed two control groups, i.e., adding different concentrations of NaCl or PEG, respectively, to the self-assembled solution, both of which ensured that the osmotic pressure of the self-assembled system could be regulated without changing the pH of the solution (Supplementary Figs. 56, 57). It was observed that the morphology of the particles formed at the four different pH did not

change significantly even when the concentration of NaCl was increased to 50 mM or the concentration of PEG was increased to 10 g/L. This indicates that the osmotic pressure was not the primary driving force for morphological transformation in the self-assembly system.

Nonlinear amplifying effect of nano bowls in response to SO₂ biosignal

We next targeted to unveil the relationship between the concavity of nano bowls and their response ability. To this end, two polymer assemblies, LCS and d-NB, with the largest shape difference, were first investigated. The LCS solution (1.0 mg/mL, containing ~ 2 mM of Cy responsive unit), in the absence of SO₂, gave a typical TPE fluorescent emission at 473 nm but had no strong intensity ($\sim 1.1 \times 10^3$ arb. units)²⁷. However, upon exposure to SO₂, the emission began to decline. When the gas level (2 mM) was equivalent to the amount of Cy groups, the fluorescence was almost silent (Fig. 5a), consistent with the quenching of the intensity of the absorption peaks observed in the UV-Vis spectral in Supplementary Fig. 60, suggesting that, as with the free polymer chains, the reaction of LCS with SO₂ still conforms to the '1-to-1' response mode. The initial fluorescence originates from the AIE effect caused by a slight aggregation of TPes, whereas the addition of SO₂ transforms the polymeric structure and breaks the chain aggregation, thus inhibiting TPE emission. For the case of d-NB solution under the same conditions, interestingly, its initial fluorescence produced a sharp increase to $\sim 8.9 \times 10^5$ arb. units, corresponding to a more compressed hydrophobic core with tighter TPE packing formed. In striking contrast to LCSs, quenching such bright fluorescence only required a trace amount of SO₂ (72 nM, 3.6×10^{-5} equiv., Fig. 5b). This means that a very small amount of Cy reacting with SO₂ is sufficient to vastly loose the overall chain aggregation state, resulting in a full shutdown of TPE emitting. Based on this, we further examined the fluorescent intensity change of nano bowls of diverse shapes before and after treating with a fixed level of SO₂ (1‰ equiv. to Cy unit). It is clear that the $I_{\text{bef}}/I_{\text{aft}}$ value displayed an exponential growth by 4 orders of magnitude with surface concaving degree (Fig. 5c). This result was also evidenced by fluorescent monitoring with SO₂ concentration. The on-off illuminated

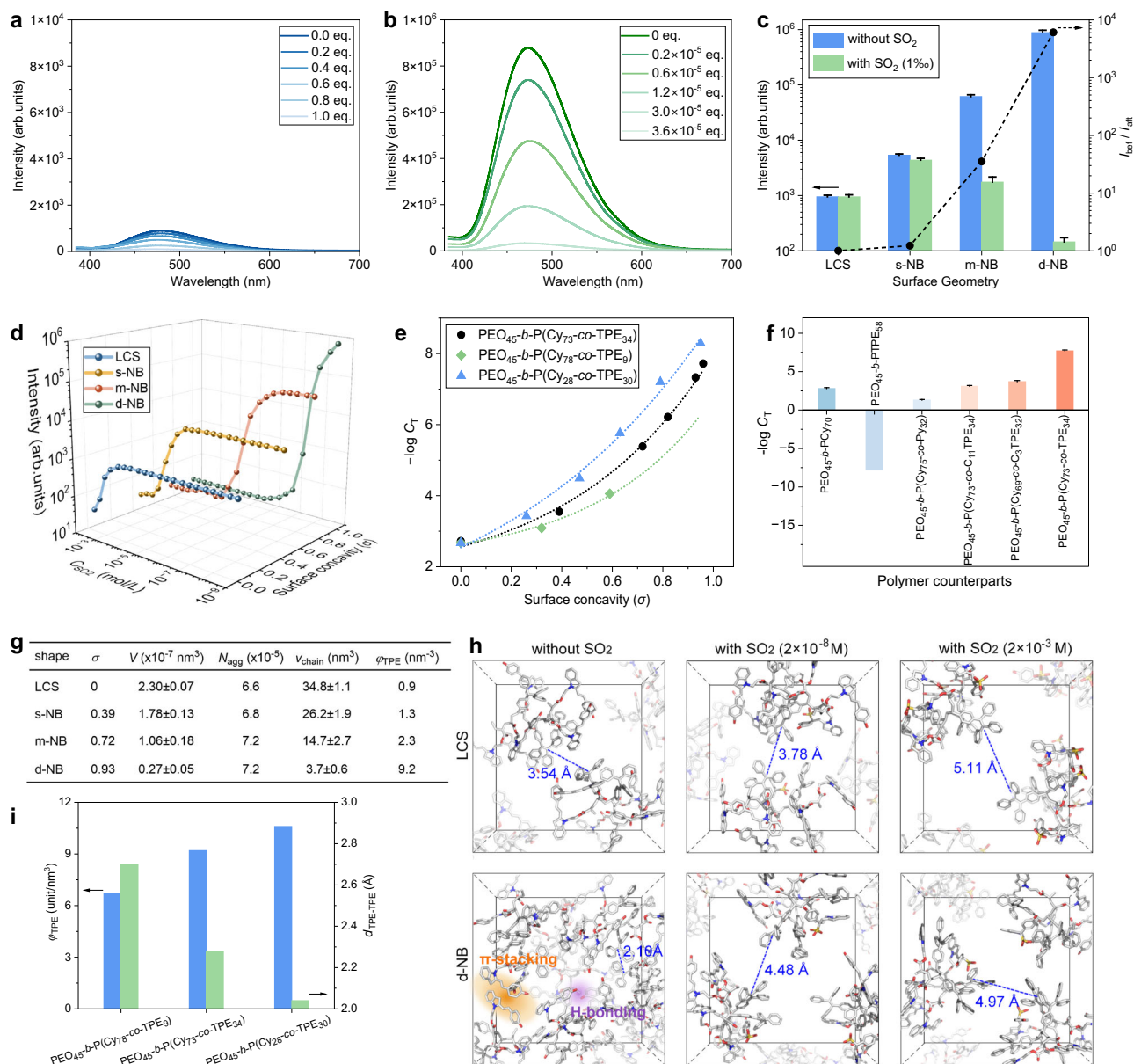


Fig. 5 | Nonlinear amplification of nano bowls to SO₂ biosignal. The fluorescent spectral change of (a) LCS and (b) d-NB assembled from PEO₄₅-b-P(Cy₇₃-co-TPE₃₄) with SO₂ concentration. c Fluorescence intensity transition of four assemblies of different morphologies before and after treating with a fixed concentration of SO₂ (1%). d Fluorescence intensity plotted versus SO₂ concentration of four assemblies of diverse surface concavity: LCSs (blue), s-NBs (yellow), m-NBs (red), and d-NBs (green). e C_T logarithmic value as a function of surface concavity (σ) under different block compositions: PEO₄₅-b-P(Cy₇₃-co-TPE₃₄) (black circle), PEO₄₅-b-P(Cy₇₈-co-TPE₉) (green diamond), and PEO₄₅-b-P(Cy₂₈-co-TPE₃₀) (blue triangle). f The comparison of C_T among the designed polymer counterparts: PEO₄₅-b-PCy₇₀, PEO₄₅-b-

PTPE₅₈, PEO₄₅-b-P(Cy₇₅-co-Py₃₂), PEO₄₅-b-P(Cy₇₃-co-C₁₁TPE₃₄), PEO₄₅-b-P(Cy₆₉-co-C₃TPE₃₂), and PEO₄₅-b-P(Cy₇₃-co-TPE₃₄) as reference (from left to right). All the polymer concentrations were kept at 1.0 mg/mL to guarantee an identical Cy amount. The error bars in (e, f) are the standard deviation of the mean. g Calculated geometric parameters of four types of polymer assemblies. h Molecular simulation of chain aggregation states in LCS and d-NB assemblies under different SO₂ concentration conditions: without SO₂ (left panels), with a small amount of SO₂ (middle panels), and with an excessive amount of SO₂ (right panels). i Comparison of TPE unit density and their group distance under different block compositional conditions.

switching of four nano bowl-like morphologies (LCS, s-NB, m-NB, and d-NB), corresponding to σ of 0, 0.39, 0.72, and 0.93, occurred at bio-signal levels of 2×10^{-3} M, 3.4×10^{-4} M, 2.7×10^{-6} M, and 1.9×10^{-8} M, respectively (Fig. 5d). If defining this transition point of fluorescent intensity as the critical response threshold (C_T) of polymer assemblies to SO₂, its negative logarithm shows a power exponential function with the nano bowl concavity, and its extreme value can attain 19 nM, matching the minimal of intracellular SO₂ level (Fig. 5e, black circles). In other words, when the surface concavity undergoes a linear increase from 0 to 1, the response-ability of our assemblies can be amplified

nonlinearly by a factor of $\sim 10^5$ (C_T , from millimole down to nanomole level). These findings demonstrate that the geometry of block copolymer assemblies can effectively improve the responsivity to biosignals in a nonlinear manner.

In a similar way, we also compared the detection limit of another two copolymers with different TPE ratios. Smaller NBs formed from PEO₄₅-b-P(Cy₂₈-co-TPE₃₀) gave a steeper C_T growing profile as a function of surface concavity than that of PEO₄₅-b-P(Cy₇₃-co-TPE₃₄) (Fig. 5e, blue triangle; Supplementary Fig. 62). One intuitive reason is that the smaller the NB volume is, the more crowded the internal chains

arrange, consequently, a lower level of SO₂ can also cause strong inhibition on TPE aggregation. On the contrary, NBs assembled by PEO₄₅-*b*-P(Cy₇₈-*co*-TPE₉) showed higher C_T under the identical surface concavity (Fig. 5e, green rhombus; Supplementary Fig. 63), which is ascribed to the less TPE moieties in per chain. Additionally, we studied the SO₂ responsiveness of those polymer counterparts. As shown in Fig. 5f, using PEO₄₅-*b*-P(Cy₇₃-*co*-TPE₃₄) as a reference, none of them can lead to a nonlinear signal gain because of the lack of TPE reporters (PEO₄₅-*b*-PCy₇₀, -lgC_T = 2.8), Cy responsive groups (PEO₄₅-*b*-PTPE₅₈, -lgC_T < 0), and no AIE property (PEO₄₅-*b*-P(Cy₇₅-*co*-Py₃₂), -lgC_T = 1.3), as well as low degree of inward invagination (PEO₄₅-*b*-P(Cy₆₉-*co*-C₃TPE₃₂), -lgC_T = 3.7; PEO₄₅-*b*-P(Cy₇₃-*co*-C₁₁TPE₃₄), -lgC_T = 3.1).

Mechanistic insight on nonlinear signal amplification by surface concavity of nano bowls

The above experiments confirm that surface concavity is indeed the crucial parameter to regulating the response-ability of polymer assemblies. To unravel the mechanism underlying this phenomenon, we combined theoretical calculation and simulation. It is known that the ability to respond to SO₂ biosignal relies upon the fluorescent mutation of polymer assemblies, while its fluorescence rests mainly on the extent of TPE aggregation. Hence, we speculated that the surface concavity could determine different changes in TPE interacting domains before and after the SO₂ trigger, which is the main reason for distinct signal response modes. For this purpose, we first analyzed the density of TPE unit in four polymer assembling morphologies (Fig. 5g and Supplementary Fig. 64). According to their geometric difference, as the surface becomes more concave from LCS to d-NB, the total volume (*V*) of each nanoparticle has a remarkable descent from 2.30 × 10⁻⁷ to 0.27 × 10⁻⁷ nm³. Static light scattering (SLS) test showed that there is only little change in their apparent molecular aggregation number per particle (*N*_{agg}) around 6.6–7.2 × 10⁵ (Supplementary Fig. 65). Thus, the number of TPE per unit volume (φ_{TPE}) can be evaluated from *V* and *N*_{agg} by Eq. (2), where *N* is the degree of polymerization of TPE.

$$\varphi_{TPE} = N_{agg} \cdot N / V \quad (2)$$

From Fig. 5g, for the case of LCSs, TPE groups in hydrophobic core adopt a loose arrangement ($\varphi_{TPE} = 0.9$ unit/nm³); in contrast, highly dense aggregation happens in the case of d-NBs, and its φ_{TPE} has a 10-fold increase to 9.2 unit/nm³. This difference in initial TPE density interprets why the initial fluorescent intensity of the assemblies varies by orders of magnitudes (LCSs: 1.1 × 10³ arb. units, d-NBs: 8.9 × 10⁵ arb. units). Molecular simulation further supported this point (Fig. 5h): in the absence of SO₂, when the assemblies deform from LCS to d-NB, the chain crowdedness in unit volume improves abruptly, and the distance between two TPE groups belonging to different chains is highly compressed from 3.54 Å to 2.10 Å, and meanwhile, this compression promotes the emergence of H-bonding and π - π interacting domains (left panels). However, introducing a trace amount of SO₂ (2 × 10⁻⁸ M, critical threshold for d-NB) leads to distinct influences on tuning TPE aggregation behavior in the two assembly forms (middle panels). For d-NBs, once a very small number of sulfonate groups formed on each chain, the electrostatic repulsion can greatly break the TPE aggregating domains and enlarge their molecular spacing (2.10 Å → 4.48 Å), which is enough to quench the TPE fluorescence. In striking contrast, for LCSs, due to the longer TPE spacing at the beginning, the increase of inter-chain TPE distance is too slight (3.54 Å → 3.78 Å) to change the emission. Only when an excess of SO₂ (2 × 10⁻³ M) is added, all the double bonds can be converted to negatively charged sulfonates, which highly reduces the TPE aggregation in LCSs, so that their extended TPE spacing (5.11 Å) is sufficient to turn off the TPE emission (right panels). The slight expansion of the bowl-shaped particles observed in the electron microscope images provides experimental evidence for the increase in

molecular spacing observed in the theoretical simulations described above (Supplementary Fig. 61). This intrinsic mechanism-driven transition of response mode of assemblies from linear output to nonlinear gain with the increase of surface concavity is impressive.

Given that the differences in TPE density and their group distance (*d*_{TPE-TPE}) are two decisive factors to control over the responsive limit, thus the C_T varying with block composition is also explainable. For NBs formed by PEO₄₅-*b*-P(Cy₇₈-*co*-TPE₉), because its initial φ_{TPE} and *d*_{TPE-TPE} are, respectively, calculated to be 6.7 unit/nm³ and 2.70 Å, this leads to a higher detection limit as compared to that of PEO₄₅-*b*-P(Cy₇₃-*co*-TPE₃₄). However, in the case of PEO₄₅-*b*-P(Cy₂₈-*co*-TPE₃₀), its reduced volume results in a more compact core, with a bigger φ_{TPE} of 10.6 but shorter *d*_{TPE-TPE} of 2.04 Å, which improves the response-ability (Fig. 5i). Furthermore, by plotting the above-obtained fluorescence intensities of different groups with their corresponding φ_{TPE} and *d*_{TPE-TPE}, respectively, it can also be revealed that the nonlinear increase in fluorescence intensity with φ_{TPE} and *d*_{TPE-TPE} is a significant contributing factor to the aforementioned enhancement of response-ability (Supplementary Fig. 66). In conjunction with the nonlinear growth presages in surfaces concavity with decreasing pH, this phenomenon contributes to the nonlinear amplification effect of surfaces concavity of nano bowls on biosignals.

Discussion

Developing an efficient nanoplatfrom to detect and monitor the level and distribution of biological signals in the cell milieu is crucial to biomedicine and theranostics. In the face of the challenge of how to respond to extremely low concentrations of biosignals in the cell milieu, we have developed a bowl-shaped polymer self-assembly nanosystem that enables nonlinear amplification to biosignal stimuli and improves the critical response limit of polymer entities by more than 5 orders of magnitude to nanomolar level, matching the scope of physiological concentrations of various biosignals in vivo. Moreover, we have first demonstrated that there exists a quantitative relationship between the nano bowls morphology and the response-ability of polymers. The response threshold behaves as an exponential growth with the surface concavity. The underlying mechanism is established on the collective impact of a single signal on transitioning the polymer chain aggregation state of individual assemblies, rather than just the conversion of a unit or chain, which makes the signal input-to-function output follow a 1-to-Nⁿ augmentation mode. This nonlinear signal gain approach has the potential to be generalizable to a variety of other biosignals and will offer a promising avenue for designing highly sensitive stimuli-responsive polymer materials.

Methods

Materials

4-vinylphenylboric acid (95%), methyl methacrylate (99%), tetrabutylammonium tribromide (TBAB, 98%), pyrene-1-carboxaldehyde (Py, 99%), tetrakis(triphenylphosphine) palladium (Pd(PPh₃)₄, 99.9%), methyl triphenylphosphine bromide (98%), 11-bromo-1-undecanol (98%), potassium iodide (KI, 99%), and gluconolactone (98%) were purchased from Sigma-Aldrich Trading Co. Ltd. (Germany). Bromotriphenylethylene (98%), 4-(1,2,2-triphenylvinyl) phenol (TPE-OH, 97%), 3-bromo-1-propanol (98%), triethylamine (99%), sodium hydride (NaH, 60% dispersion in mineral oil), and potassium carbonate (K₂CO₃, 99%) were obtained from Aladdin Biochemical Technology Co. Ltd. (Shanghai, China). Poly(ethylene oxide) macro-based chain transfer agent (PEO-CTA) for RAFT polymerization was synthesized by our previous method. SO₂-sensitive monomer *E*-3-(2-(4-hydroxystyryl)-(2-hydroxyethyl)-3,3-dimethyl-3H-indoline methacrylate (Cy) functional monomer was prepared in three steps according to previous literature (yield: 45%)²⁶. All the solvents for product purification and self-assembly process, including dimethyl formamide (DMF), dichloromethane (CH₂Cl₂), tetrahydrofuran (THF), methanol (CH₃OH), ethyl

acetate, *n*-hexane, and toluene were purchased from Shanghai Chemical Ltd. Co. The solvents for anhydrous reactions or polymerizations including CH_2Cl_2 , acetonitrile (CH_3CN), and DMF were purified by the Innovative Technologies Solvent Purification System and were degassed via three cycles of freeze-pump-thaw operation prior to use. Unless stated elsewhere, the other reagents used were of analytical or high-performance liquid chromatography (HPLC) grade.

Instruments and characterization

Nuclear magnetic resonance (NMR) spectroscopy was performed on an AVANCE III HD 400 MHz of Bruker BioSpin International Instrument. Tetramethylsilane (TMS) was utilized as an internal standard, and CDCl_3 , CD_3CN , CD_2Cl_2 , or $\text{DMSO}-d_6$ were used as the NMR solvents at room temperature to probe ^1H NMR (400 MHz) and ^{13}C NMR (100 MHz) spectra of all the target compounds and polymers. Gel permeation chromatograph (GPC) adopted a Waters-515 system, equipped with a Waters degasser, a HPLC pump, and a Wyatt DSP refractive index (RI) detector. The molecular weights (M_n , M_w) and polydispersity (\bar{D}) for all the polymer samples were evaluated by the GPC system. It contains one Styragel guard column (7.5×50 mm), a Styragel HR3 column ($5 \mu\text{m}$, 7.8×300 mm, M_n range: $500 - 3 \times 10^4$ g/mol), and a Styragel HR5E column ($5 \mu\text{m}$, 7.8×300 mm, M_n range: $2 \times 10^3 - 4 \times 10^6$ g/mol), in which HPLC-grade THF was used as the eluent (flow rate of 1.0 mL/min at 50°C) and polystyrene (PS) series as the standards for calibration (M_n measuring range: 650 - 826,000 g/mol). Matrix-assisted laser desorption/ionization time-of-flight mass spectroscopy (MALDI-TOF) was performed on an Autoflex II TOF/TOF mass spectrometer (Bruker Daltonik GmbH) system. The instrument is equipped with a 337 nm nitrogen laser. All the samples were dissolved in a solution of THF and mixed with a matrix solution, *trans*-2-[3-(4-*tert*-butylphenyl)-2-methyl-2-propenylidene] (DCTB) matrix and sodium trifluoroacetate ionization reagent. Dynamic light scattering (DLS) experiments were performed by a Zetasizer Nano ZS90 from Malvern Instrument with a 4 mW He-Ne 633 nm laser module operating at 25°C . Tests were carried out at an angle of 173° , and the data was analyzed by Malvern DTS v7.03 software. All the measurements were repeated three times, with at least 10 rounds recorded for each run. The hydrodynamic diameter (D_h) of the polymer assembly was calculated by the Stokes-Einstein equation, $D_h = k_B T / 3\pi\eta D$, where particles are assumed to be the spherical shape and k_B represents the Boltzmann constant, T as the absolute temperature, η as the solvent viscosity and D as the solvent diffusion coefficient. Transmission electron microscopy (TEM) was recorded on an FEI Tecnai G2-T20 S-TWIN instrument at 120 kV equipped with an AMT 16-megapixel in-line CCD camera. All TEM samples were prepared as follows. The aqueous solutions of polymer assemblies (3.0 μL) were dropped onto a copper grid for 1 min and then blotted with filter paper to remove excess solution, followed by drying overnight in a vacuum oven at ambient temperature. These grids were used for imaging without staining. Scanning electron microscope (SEM) was employed a Zeiss Gemini SEM500 electron microscope. All the polymer assembly solutions (3.0 μL) were dropped onto plasma-pretreated silicon substrates and dried. Before observation, the surface of silicon substrates was also sputtered with a thin layer of Au (10 mA, 60 s) to increase the electrical conductivity. Atomic force microscope (AFM) was carried out on a Dimension-ICON Scanning probe Microscope (Bruker, Digital Instrument Co. Ltd.) equipped with a MikroMasch silicon cantilever, NSCII (radius < 10 nm, resonance frequency = 300 kHz, spring constant = 40 N/m) with tapping mode at room temperature. The polymer self-assembly samples for AFM observation were prepared by depositing drops of the polymer solutions (10 μL) onto the freshly exfoliated mica and after the excess solution was removed with a spin coater. The samples were freeze-dried at -50°C for 24 h by vacuum before measurement. Fourier transform infrared spectroscopy (FT-IR) was measured on a Perkin-Elmer Spotlight 400 FT-IR system. The polymer assemblies underwent freeze-dried operation first and used

their solid powders to proceed with resonance scanning at the range of $500 - 4000 \text{ cm}^{-1}$. Differential scanning calorimetry (DSC) was employed to measure the glass transition temperatures (T_g) of PEO-*b*-PCy, PCy, and PTPE using a DSC Q2000 (TA Instruments). During the DSC measurement, the polymer powder was kept for 2 min at -20°C , heated at the rate of $10^\circ\text{C}/\text{min}$ to 150°C and cooled at the rate of $10^\circ\text{C}/\text{min}$ to -20°C . This cycle was repeated twice, and TA Universal Analysis Software was used to analyze the last heating curve to calculate the T_g .

Synthesis of tetraphenyl ethylene-based functional monomer (TPE)

The TPE monomer was synthesized as referring to a previously reported method as shown in Supplementary Fig. 1a⁵⁴. Under nitrogen protection, bromotriphenylethylene (2.03 g, 6.0 mmol), 4-vinylphenylboric acid (1.07 g, 7.2 mmol), and tetrabutylammonium tribromide (0.29 mg, 0.6 mmol) were added to a 250 mL three-neck flask and dissolved in 40 mL of toluene. Then 10 mL of potassium carbonate aqueous solution (~ 2 M) was added to the above solution and stirred for 1 h, followed by adding $\text{Pd}(\text{PPh}_3)_4$ catalyst (8 mg, 7 μmol). The reaction was heated to 85°C for 24 h and then cooled to room temperature. After removing the toluene solvent via reduced evaporation, the organic phase was extracted with CH_2Cl_2 and deionized water twice, and followed by dried with anhydrous magnesium sulfate. The crude product was purified by silica gel chromatography (*n*-hexane) to give a white solid powder product (1.93 g, yield: 90%). The structure was confirmed by ^1H NMR, ^{13}C NMR, and MALDI-TOF spectroscopy (Supplementary Figs. 2–4). ^1H NMR (CDCl_3): δ (ppm) = 6.95 - 7.18 (m, 19H), 6.57 - 6.67 (dd, 1H, $J = 10.92$ Hz, 17.60 Hz), 5.65 (d, 1H, $J = 17.60$ Hz), 5.17 (d, 1H, $J = 11.00$ Hz); ^{13}C NMR (CDCl_3): δ (ppm) = 143.78, 143.41, 141.09, 140.62, 136.63, 135.55, 131.37, 127.79, 126.51, 125.58, 113.49; MALDI-TOF (m/z): calcd. $\text{C}_{28}\text{H}_{22} [\text{M} + \text{H}]^+$, 358.48; found, 358.30.

Synthesis of 3-(4-(1,2-triphenylvinyl)phenoxy)propan-1-ol (TPE-C₃-OH)

The TPE-based other monomers with a short aliphatic spacer were prepared as the control compound, as shown in Supplementary Fig. 1b⁵⁵. TPE-OH (1.04 g, 3.0 mM), 3-bromo-1-propanol (0.33 mL, 3.6 mM), and K_2CO_3 (0.83 g, 6.0 mM) were added to 20 mL of dried CH_3CN solution. The reaction mixture was then heated to reflux for 18 h. After cooling to room temperature, the insoluble salts were removed by filtration, followed by removing the solvent with reduced evaporation. The residue was purified on silica gel chromatography (*n*-hexane/acetate, 3/1, v/v) as the eluent to afford a pure white solid powder product (0.70 g, yield: 57%). The structure was confirmed by ^1H NMR, ^{13}C NMR, and MALDI-TOF spectroscopy (Supplementary Figs. 5–7). ^1H NMR (CDCl_3): δ (ppm) = 7.18 - 7.03 (m, 15H), 6.96 (d, 2H, $J = 8.76$ Hz), 6.68 (d, 2H, $J = 8.8$ Hz), 4.06 (t, 2H, $J = 5.92$ Hz), 3.84 (t, 2H, $J = 5.92$ Hz), 2.11 (s, 1H), 2.01 (q, 2H, $J = 5.88$ Hz); ^{13}C NMR (CDCl_3): δ (ppm) = 157.24, 143.91, 140.43, 140.09, 136.26, 132.53, 127.70, 127.57, 126.23, 113.54, 65.39, 60.28, 31.94; MALDI-TOF (m/z): calcd. $\text{C}_{29}\text{H}_{26}\text{O}_2 [\text{M} + \text{H}]^+$, 406.53; found, 406.35.

Synthesis of TPE-based monomeric analog with short C₃ spacer (C₃TPE)

The above-obtained TPE-C₃-OH (0.60 g, 1.48 mM) was dissolved in 10 mL of CH_2Cl_2 , followed by the addition of triethylamine (0.62 mL, 4.43 mM) in an ice bath. Methyl methacrylate (0.18 mL, 1.77 mM) was dissolved in 5 mL of CH_2Cl_2 and then slowly added to the reaction system under nitrogen protection. Removing the ice bath after the ice melted naturally, and then the reaction was stirred at room temperature overnight. After the reaction ended and was detected by TCL, the reactive solution was washed with dilute hydrochloric acid aqueous solution (0.1 M) and brine to remove the water-soluble byproducts from the system. The collected organic phases were then dried and concentrated by evaporation. Purified by silica column chromatography

(*n*-hexane/acetate, 3/1, v/v) as the eluent, a final yellowish product was obtained (0.38 g, yield: 80%). The structure was confirmed by ^1H NMR, ^{13}C NMR, and MALDI-TOF spectroscopy (Supplementary Figs. 8–10). ^1H NMR (CDCl_3): δ (ppm) = 7.15–6.97 (m, 15H), 6.91 (d, 2H, J = 8.76 Hz), 6.61 (d, 2H, J = 8.8 Hz), 6.09 (s, 1H), 5.56 (t, 1H, J = 1.56 Hz), 4.31 (t, 2H, J = 6.32 Hz), 3.99 (t, 2H, J = 6.16 Hz), 2.01 (q, 2H, J = 5.2 Hz), 1.93 (s, 3H); ^{13}C NMR (CDCl_3): δ (ppm) = 167.37, 157.26, 143.99, 140.10, 136.24, 132.52, 131.31, 129.05, 127.58, 126.23, 125.52, 113.54, 64.20, 61.58, 28.67, 18.32; MALDI-TOF (m/z): calcd. $\text{C}_{33}\text{H}_{30}\text{O}_3$ [$\text{M} + \text{H}$] $^+$, 474.60; found, 474.41.

Synthesis of 11-(4-(1,2,2-triphenylvinyl)phenoxy)undecan-1-ol (TPE- C_{11} -OH)

The TPE-based another monomer with a long aliphatic spacer was prepared as the control compound, as shown in Supplementary Fig. 1c. K_2CO_3 (0.78 g, 5.6 mM), 11-bromo-1-undecanol (0.84 g, 3.4 mM), KI (2.3 mg, 0.014 mM) were added to the TPE-OH compound (1.04 g, 2.8 mM) in DMF solution and stirring vigorously. Then the mixture was heated to 100 °C for 10 h. Afterward, the organic solvent was removed by rotary evaporation, and the residual was extracted with CH_2Cl_2 and deionized water twice, followed by collecting the organic phases and drying with anhydrous magnesium sulfate. Finally, the crude product was purified by silica gel chromatography (*n*-hexane/acetate, 10/1, v/v) as the eluent to obtain a pure product (0.73 g, yield: 44%). The structure was confirmed by ^1H NMR, ^{13}C NMR, and MALDI-TOF spectroscopy (Supplementary Figs. 11–13). ^1H NMR (CDCl_3): δ (ppm) = 7.14–7.00 (m, 15H), 6.93 (d, 2H, J = 8.64 Hz), 6.64 (d, 2H, J = 8.64 Hz), 3.87 (t, 2H, J = 6.56 Hz), 3.64 (t, 2H, J = 6.68 Hz), 1.74 (q, 2H, J = 6.64 Hz), 1.59 (q, 3H, J = 5.83 Hz), 1.31 (m, 14H); ^{13}C NMR (CDCl_3): δ (ppm) = 157.69, 144.03, 140.60, 139.97, 135.88, 132.50, 131.37, 127.58, 126.20, 113.56, 67.79, 63.04, 60.42, 32.80, 29.43, 26.07, 25.76; MALDI-TOF (m/z): calcd. $\text{C}_{37}\text{H}_{42}\text{O}_2$ [$\text{M} + \text{H}$] $^+$, 518.74; found, 518.50.

Synthesis of TPE-based monomeric analog with long C_{11} spacer (C_{11} TPE)

The above-prepared TPE- C_{11} -OH (0.73 g, 1.41 mM) was dissolved in 10 mL of CH_2Cl_2 dichloromethane, followed by the addition of triethylamine (0.59 mL, 4.23 mM) in an ice bath. Methyl methacrylate (0.17 mL, 1.70 mM) was dissolved in 5 mL of CH_2Cl_2 and then slowly added to the reaction system under nitrogen protection. Removing the ice bath after the ice melted naturally, and the reaction was stirred at room temperature overnight. After the reaction ended and detected by TLC, the residual was washed with dilute acid and brine to remove the water-soluble byproducts from the system. The collected organic phases were then dried and concentrated, followed by purified by silica gel chromatography with (*n*-hexane/acetate, 4/1, v/v) to obtain the final yellowish product (0.46 g, yield: 78%). The structure was confirmed by ^1H NMR, ^{13}C NMR, and MALDI-TOF spectra (Supplementary Figs. 14–16). ^1H NMR (CDCl_3): δ (ppm) = 7.13–6.98 (m, 15H), 6.90 (d, 2H, J = 8.76 Hz), 6.63 (d, 2H, J = 8.76 Hz), 6.09 (s, 1H), 5.54 (s, 1H), 4.14 (t, 2H, J = 6.68 Hz), 3.86 (t, 2H, J = 6.56 Hz); ^{13}C NMR (CDCl_3): δ (ppm) = 167.61, 157.69, 144.03, 132.50, 131.34, 129.05, 127.58, 126.20, 125.18, 113.56, 67.81, 64.86, 29.53, 28.62, 25.99; MALDI-TOF (m/z): calcd. $\text{C}_{41}\text{H}_{46}\text{O}_3$ [$\text{M} + \text{H}$] $^+$, 586.82; found, 586.55.

Synthesis of pyrene-based fluorescent monomeric counterpart 1-vinyl pyrene (Py)

1-Vinyl pyrene was synthesized according to the previous literature with some modifications (Supplementary Fig. 1d)³⁶. NaH (0.22 g, 5.4 mmol) and methyltriphenylphosphine bromide (1.61 g, 4.5 mmol) were dissolved in 20 mL of THF under nitrogen protection and heated at 50 °C for 1 h. The THF solution of pyrene-1-carboxaldehyde (0.69 g, 3.0 mmol) was subsequently added, and the solution was restored to room temperature for reaction overnight. After quenching and neutralizing the reaction with dilute hydrochloric acid aqueous solution, the organic phase was extracted with CH_2Cl_2 and dried. The concentrated solution

was purified by silica gel chromatography (*n*-hexane/acetate, 40/1, v/v) to obtain the pure product (0.51 g, yield: 75%). The structure was confirmed by ^1H NMR, ^{13}C NMR, and MALDI-TOF spectra (Supplementary Figs. 17–19). ^1H NMR (CDCl_3): δ (ppm) = 8.37–8.41 (dd, 1H, J = 9.28 Hz), 7.98–8.23 (m, 8H), 7.75–7.84 (dd, 1H, J = 11.00 Hz, 17.24 Hz), 6.02 (d, 1H, J = 18.56 Hz), 5.63 (d, 1H, J = 12.24 Hz); ^{13}C NMR (CDCl_3): δ (ppm) = 134.26, 132.42, 131.50, 130.94, 127.62, 127.48, 127.32, 125.99, 125.29, 125.06, 124.51, 123.73, 123.08, 123.08, 117.28; MALDI-TOF (m/z): calcd. $\text{C}_{18}\text{H}_{12}$ [$\text{M} + \text{H}$] $^+$, 228.29; found, 228.20.

RAFT polymerization of PEO-*b*-P(Cy-*co*-TPE) block copolymer

The target block copolymer PEO-*b*-P(Cy-*co*-TPE) was prepared by RAFT polymerization according to the literature elsewhere (Supplementary Fig. 20a), in which the PEO-based macro-chain transfer agent (PEO-CTA) and the SO_2 -sensitive cyanine-based functional monomer (Cy) were successfully synthesized from the methods reported in our previous work²⁶. Typically, PEO₄₅-CTA (0.022 g, 10 μmol , 1.0 equiv., The subscript represents the degree of polymerization), Cy monomer (0.30 g, 0.8 mmol, 80 equiv.) and TPE monomer (0.072 g, 0.2 mmol, 40.0 equiv.) were dissolved in 1 mL of anhydrous DMF. Then 164 μL of AIBN (1.0 mg mL⁻¹ in anhydrous DMF, 0.1 equiv.) radical initiator was added, and the mixing solution was degassed by three freezing-pump-thawing cycles. The feed ratio of the initiator, macro-CTA, and two monomers was fixed at [initiator]:[CTA]:[Cy]:[TPE] = 0.1:1:80:40. After being sealed carefully, the reaction tube was placed in an oil bath at 70 °C and stirred for 10 h. Then the polymerization was quenched in liquid nitrogen. The reaction mixture was concentrated by rotary evaporation and then an excess of diethyl ether was added for precipitation, and then the precipitation and supernatant were separated by centrifugation. This dissolution-precipitation step was repeated for at least three times to finally obtain a light yellow powder (0.30 g, conversion: 79%). The polymer structure was confirmed by ^1H NMR analysis, and the number-average molecular weight (M_n), weight-average molecular weight (M_w), and polydispersity (\mathcal{D}) were determined by GPC analysis (Supplementary Figs. 21, 22 and Supplementary Table 1). $M_{n,\text{GPC}}$ = 38,000 g/mol, $M_{w,\text{GPC}}$ = 45,600 g/mol, \mathcal{D} = 1.19.

RAFT polymerization of other TPE- and Py-containing polymer controls/counterparts

In a similar way, other polymer controls, including PEO-*b*-P(Cy-*co*-C₃TPE) and PEO-*b*-P(Cy-*co*-C₁₁TPE), in which the short and long spacers were introduced to isolate the main chain and TPE group, were polymerized, respectively (Supplementary Fig. 20b, c). PEO-*b*-PCy and PEO-*b*-PTPE, which lack fluorescent units and SO_2 -sensitive functional groups, were also prepared (Supplementary Fig. 20d, e) as two polymer counterparts to indicate the point of view that the formation of bowl-shaped particles requires the simultaneous existence of Cy and TPE units. In addition, we also synthesized PEO-*b*-P(Cy-*co*-Py) block copolymer as the counterpart, where pyrene fluorophores replace the TPE ones (Supplementary Fig. 20f). The corresponding ^1H NMR spectra and block composition parameters were shown in Supplementary Figs. 23–28 and Supplementary Table 2.

RAFT polymerization of PCy homopolymer

A dried Schlenk tube equipped with a magnetic stirring bar was added with the CTA (2.73 mg, 10 μmol , 1.0 equiv.), Cy monomer (0.378 g, 0.8 mmol, 80 equiv.) and 1 mL of anhydrous DMF. Then 328 μL of AIBN (1.0 mg/mL in anhydrous DMF, 0.1 equiv.) radical initiator was added to the Schlenk tube subsequently. The feed ratio of [I]: [CTA]: [M] is 0.2:1:80. The tube was carefully degassed by three freezing-pump-thawing cycles and then sealed under vacuum. After polymerization for 10 h at 70 °C with stirring, the tube was immersed in liquid nitrogen to quench the polymerization and then returned to room temperature. Subsequently, the reaction mixture was precipitated into an excess of cold diethyl ether for three times to obtain the yellowish product

(0.13 g, conversion: 52%). The polymer structure was confirmed by ^1H NMR analysis, and the number-average molecular weight (M_n), weight-average molecular weight (M_w), and polydispersity (\mathcal{D}) were determined by GPC analysis (Supplementary Fig. 37, $M_{n,\text{GPC}} = 25,500$ g/mol, $M_{w,\text{GPC}} = 33,400$ g/mol, $\mathcal{D} = 1.31$).

RAFT polymerization of PTPE homopolymer

A dried Schlenk tube equipped with a magnetic stirring bar was added with the CTA (2.73 mg, 10 μmol , 1.0 equiv.), TPE monomer (0.107 g, 0.3 mmol, 30 equiv.), and 1 mL of anhydrous DMF. 328 μL of AIBN (1.0 mg/mL in anhydrous DMF, 0.1 equiv.) radical initiator was added to the Schlenk tube subsequently. The feed ratio of [I]: [CTA]: [M] is 0.2:1:30. The tube was carefully degassed by three freezing-pump-thawing cycles and then sealed under vacuum. After polymerization for 10 h at 70 $^\circ\text{C}$ with stirring, the tube was immersed in liquid nitrogen to quench the polymerization and then returned to room temperature. Subsequently, the reaction mixture was precipitated into an excess of cold diethyl ether for three times to obtain the yellowish product (0.06 g, conversion: 64%). The polymer structure was confirmed by ^1H NMR analysis, and the number-average molecular weight (M_n), weight-average molecular weight (M_w), and polydispersity (\mathcal{D}) were determined by GPC analysis (Supplementary Fig. 38, $M_{n,\text{GPC}} = 10,100$ g/mol, $M_{w,\text{GPC}} = 12,400$ g/mol, $\mathcal{D} = 1.23$).

Visualization of nano bowls by cryogenic transmission electron microscope (Cryo-TEM)

Cryo-TEM images were acquired on a Cryo ARM 300 cryo-transmission electron microscope operating at an acceleration voltage of 300 kV under conditions with a Gatan 626 cryo holder. Samples were first prepared on Vitrobot by depositing 5 μL sample solution onto Quantifoil porous carbon grid (300 mesh, R2/2, which had been pre-treated with a glow discharger to increase its hydrophilicity), and the excess solvent was removed by filter paper (blot time was 3 seconds). Then, the copper grid was quickly plunged into a pool of liquid ethane, which was cooled down at liquid nitrogen temperature to vitrify the samples. Finally, the copper grid was transferred through a pre-cooled magazine into a cryo-transmission electron microscope, and the rapidly frozen samples were observed using Gatan's K3 camera in low-dose mode. The images were recorded on a 4 K \times 4 K CCD digital camera at 52000 \times magnification.

SO₂-responsive block copolymer self-assembly process

The as-synthesized PEO-*b*-P(Cy-co-TPE) copolymers were dissolved in 1 mL of THF to give a 1.0 mg/mL solution, followed by slowly adding a variety of pH buffer in aqueous solutions (phosphate buffer, pH = 9.0, 8.3, 7.6, 6.8, 6.2, 5.5, and 5.0; dropwise rate - 0.1 mL/h) to obtain an aggregate solution (THF/H₂O, 1/1, v/v). After the aggregate formed, these solutions with diverse pH values were incubated to equilibrium for 48 h before microscopic observation and responsive investigation.

pH measurement

The pH measurement was conducted utilizing a SevenCompact S220-K benchtop pH meter (Mettler Toledo), equipped with an InLab Science-Pro ISM pH/temperature electrode. Prior to each analysis, the pH meter was calibrated using standard buffer solutions with pH values of 2.00, 4.010, 7.00, 9.21, and 11.00. Following each analysis, the pH electrodes were subjected to a repeated cleaning process. This involved immersing them in deionized water and gently wiping them with lint-free paper in order to remove any excess water. The electrodes were then immediately immersed in the solution to be measured for the next analysis.

In situ pH adjustment in self-assembled solutions

A 100 mM solution was prepared by weighing 0.178 g of gluconolactone and dissolving it in 10 mL of phosphate-buffered saline (PBS)

buffer with a pH of 8.3. Subsequently, the aforementioned solution was added to the THF solution of the PEO₄₅-*b*-P(Cy₇₃-co-TPE₃₄) copolymer to obtain the aggregation solution (THF/H₂O, 1/1, v/v). A quick mixing was done prior to pH measurement and microscopic observation of the particles in the solution.

Gas control device and gas concentration calibration

In order to quantitatively control the gas aeration amount to the polymer self-assembly solution, we regulated the gas aeration by connecting a microflow-pump HRF 1425-580 (ProStar, Praxair Co.) to a gas cylinder (4 L) of high-purity SO₂. The gas flow rate was controlled in the range of 0.002 to 2.0 mL/s, and the inlet pressure ranged from 0.1 to 1.0 MPa. The actual SO₂ concentration in the solution was calculated using the ideal gas state equation ($pV = nRT$), where p is the pressure, V is the volume of the gas, n is the amount of substance of the gas, R is the molar gas constant, and T is the temperature. To be more precise, the UV-Vis absorption measurements were also conducted at 277 nm by drumming SO₂ into an equal volume of ethanol as the assembled solution at the same inlet pressure and gas flow rate. The fresh ethanol solution of SO₂ was then immediately placed into a UV-Vis absorption spectrometer for analysis. According to Lambert's law ($A = \epsilon bc$, where A is the absorbance, ϵ is the molar absorption coefficient, b is the thickness of the absorbing layer, and c is the concentration of the absorbing substance), the molar absorption coefficient (ϵ) is equal to 365 M⁻¹cm⁻¹ in this case, allowing for the calculation of the concentration of SO₂.

Data availability

All data supporting the findings of this study are detailed in the paper and the Supplementary Materials. The raw data generated in this study have been deposited in the Figshare database under the accession code <https://doi.org/10.6084/m9.figshare.27117103>.

References

1. Alberts, B. et al. *Molecular Biology of the Cell*, 4th ed., New York (2002).
2. Basudhar, D. et al. Biological signaling by small inorganic molecules. *Coord. Chem. Rev.* **306**, 708–723 (2016).
3. Uvesky, V. N., Oldfield, C. J. & Dunker, A. K. Showing your ID: intrinsic disorder as an ID for recognition and cell signaling. *J. Mol. Recognit.* **18**, 343–384 (2005).
4. Wang, Y.-P. & Lei, Q.-Y. Metabolite sensing and signaling in cell metabolism. *Signal Transduct. Tar.* **3**, 30 (2018).
5. Dickinson, B. C. & Chang, C. J. Chemistry and biology of reactive oxygen species in signaling or stress response. *Nat. Chem. Biol.* **7**, 504–511 (2011).
6. D'Autréaux, B. & Toledano, M. B. ROS as signaling molecules: mechanisms that generate specificity in ROS homeostasis. *Nat. Rev. Mol. Cell Biol.* **8**, 813–824 (2007).
7. Collier, J. J., Oláhová, M., McWilliams, T. G. & Taylor, R. W. Mitochondrial signaling and homeostasis: from cell biology to neurological disease. *Trends Neurosci.* **46**, 137–152 (2023).
8. Hanahan, D. & Weinberg, R. A. Hallmarks of cancer: the next generation. *Cell* **144**, 646–674 (2011).
9. Von Maltzahn, G. et al. Nanoparticles that communicate in vivo to amplify tumour targeting. *Nat. Mater.* **10**, 545–552 (2011).
10. Cook, A. B. & Decuzzi, P. Harnessing endogenous stimuli for responsive materials in theranostics. *ACS Nano* **15**, 2068–2098 (2021).
11. Lu, Y., Aimetti, A. A., Langer, R. & Gu, Z. Bioresponsive materials. *Nat. Rev. Mater.* **2**, 16075 (2017).
12. Yong, H. W. & Kakkar, A. The unexplored potential of gas-responsive polymers in drug delivery: progress, challenges and outlook. *Polym. Int.* **71**, 514–520 (2022).
13. Giorgio, M., Trinei, M., Migliaccio, E. & Pelicci, P. G. Hydrogen peroxide: a metabolic by-product or a common mediator of ageing signals? *Nat. Rev. Mol. Cell Biol.* **8**, 722–728 (2007).

14. Sato, M., Hida, N. & Umezawa, Y. Imaging the nanomolar range of nitric oxide with amplifier-coupled fluorescent indicator in living cells. *Proc. Natl. Acad. Sci. USA* **102**, 14515–14520 (2005).
15. Zhang, Q. et al. Stimuli-responsive polymers for sensing and reacting to environmental conditions. *Prog. Polym. Sci.* **116**, 101386 (2021).
16. Ye, H. et al. Recent advances on reactive oxygen species-responsive delivery and diagnosis system. *Biomacromolecules* **20**, 2441–2463 (2019).
17. Criado-Gonzalez, M. & Mecerreyes, D. Thioether-based ROS responsive polymers for biomedical applications. *J. Mater. Chem. B* **10**, 7206–7221 (2022).
18. Xu, M. M., Liu, R.-J. & Yan, Q. Biological stimuli-responsive polymer systems: design, construction and controlled self-assembly. *Chin. J. Polym. Sci.* **36**, 347–365 (2018).
19. Shelef, O., Gnaim, S. & Shabat, D. Self-immolative polymers: an emerging class of degradable materials with distinct disassembly profiles. *J. Am. Chem. Soc.* **143**, 21177–21188 (2021).
20. Tan, J. J., Hu, J. M. & Liu, S. Y. Designing self-propagating polymers with ultrasensitivity through feedback signal amplification. *Polym. Chem.* **12**, 6230–6241 (2021).
21. Gnaim, S. & Shabat, D. Self-immolative chemiluminescence polymers: innate assimilation of chemiexcitation in a domino-like depolymerization. *J. Am. Chem. Soc.* **139**, 10002–10008 (2017).
22. Deng, Z. Y. & Gillies, E. R. Emerging trends in the chemistry of end-to-end depolymerization. *JACS Au* **3**, 2436–2450 (2023).
23. Stipanuk, M. H. et al. Sulfur amino acid metabolism: pathways for production and removal of homocysteine and cysteine. *Annu. Rev. Nutr.* **24**, 539–577 (2004).
24. Huang, Y. Q. et al. Endogenous sulfur dioxide is a new gaso-transmitter with promising therapeutic potential in cardiovascular system. *Sci. Bull.* **66**, 1604–1607 (2021).
25. Huang, Y. Q., Tang, C. S., Du, J. B. & Jin, H. F. Endogenous sulfur dioxide: a new member of gasotransmitter family in the cardiovascular system. *Oxid. Med. Cell. Longev.* **2016**, 8961951 (2016).
26. Li, X. F., Wang, Y. X. & Yan, Q. Cyanine polymersomes in breathe gas signaling molecule: SO₂-driven bilayer tubular deformation for transmembrane traffic regulation. *Angew. Chem. Int. Ed.* **62**, e202305290 (2023).
27. Zhang, N. et al. Fluorescent polymersomes with aggregation-induced emission. *ACS Nano* **12**, 4025–4035 (2018).
28. Cao, S. P. et al. Cucurbit-like polymersomes with aggregation-induced emission properties show enzyme-mediated motility. *ACS Nano* **15**, 18270–18278 (2021).
29. Jain, S. & Bates, F. S. On the origins of morphological complexity in block copolymer surfactants. *Science* **300**, 460–464 (2000).
30. Kim, H., Kang, Y. J., Kang, S. & Kim, K. T. Monosaccharide-responsive release of insulin from polymersomes of polyboroxole block copolymer at neutral pH. *J. Am. Chem. Soc.* **134**, 4030–4033 (2012).
31. Hu, J. M. et al. Biomimetic polymers responsive to biological signaling molecule: nitric oxide triggered reversible self-assembly of single macromolecular chains into nanoparticles. *Angew. Chem. Int. Ed.* **53**, 7779–7784 (2014).
32. Yan, Q. & Sang, W. H₂S gasotransmitters-responsive polymer vesicles. *Chem. Sci.* **7**, 2100–2105 (2016).
33. Huang, Y. Q. et al. Sulfur dioxide: endogenous generation, biological effects, detection, and therapeutic potential. *Antioxid. Redox Signal.* **36**, 256–274 (2022).
34. Wang, J. et al. Revealing mitochondrion-lysosome dynamic interactions and pH variations in live cells with a pH-sensitive fluorescent probe. *Anal. Chem.* **95**, 16609–16617 (2023).
35. Jiang, J. et al. π - π Interlocking effect for designing biodegradable nanorod with controlled lateral surface curvature. *Chem. Mater.* **34**, 4937–4945 (2022).
36. Zhang, M. X. et al. Pyrene-based nonwoven fabric with tunable fluorescence properties by employing the aggregation-caused quenching effect. *ACS Appl. Mater. Interfaces* **13**, 9036–9042 (2021).
37. Zhang, Y. J. et al. Reversible fluorescent probe for selective detection and cell imaging of oxidative stress indicator bisulfite. *Anal. Chem.* **88**, 4426–4431 (2016).
38. Mai, Y. & Eisenberg, A. Self-assembly of block copolymers. *Chem. Soc. Rev.* **41**, 5969–5985 (2012).
39. Qi, W. W. & Zhou, Y. F. Multimicelle aggregate mechanism for spherical multimolecular micelles: from theories, characteristics and properties to applications. *Mater. Chem. Front.* **3**, 1994–2009 (2019).
40. Sun, H. et al. Polymeric bowl-shaped nanoparticles: hollow structures with a large opening on the surface. *Macromol. Rapid Commun.* **44**, 2300196 (2023).
41. Pal, D. et al. Nanobowls from amphiphilic core-shell cyclic bottle-brush polymers. *Macromolecules* **55**, 7446–7453 (2022).
42. Panzarasa, G. et al. Supramolecular assembly by time-programmed acid autocatalysis. *Mol. Syst. Des. Eng.* **5**, 445–449 (2020).
43. Adams, D. J. et al. A new method for maintaining homogeneity during liquid–hydrogel transitions using low molecular weight hydrogelators. *J. Soft Matter* **5**, 1856–1862 (2009).
44. Panzarasa, G. Clocking the clock: Programmable acid autocatalysis in the chlorite-tetrathionate Reaction. *ChemistrySelect* **5**, 8074–8077 (2020).
45. Engin, K. et al. Extracellular pH distribution in human tumours. *Int. J. Hyperth.* **11**, 211–216 (1995).
46. Sun, H., Liu, D. Q. & Du, J. Z. Nanobowls with controlled openings and interior holes driven by the synergy of hydrogen bonding and π - π interaction. *Chem. Sci.* **10**, 657–664 (2019).
47. Hestand, N. J. & Spano, F. C. Expanded theory of H- and J-molecular aggregates: the effects of vibronic coupling and intermolecular charge transfer. *Chem. Rev.* **118**, 7069–7163 (2018).
48. Wu, T. et al. Homopolymer nanobowls with a controlled size and denting degree. *Polym. Chem.* **13**, 1236–1242 (2022).
49. Abeilmohsen, L. K. E. A. et al. Formation of well-defined, functional nanotubes via osmotically induced shape transformation of biodegradable polymersomes. *J. Am. Chem. Soc.* **138**, 9353–9356 (2016).
50. Rikken, R. S. M. et al. Shaping polymersomes into predictable morphologies via out-of-equilibrium self-assembly. *Nat. Commun.* **7**, 12606 (2016).
51. Kim, K. T. et al. Polymersome stomatocytes: Controlled shape transformation in polymer vesicles. *J. Am. Chem. Soc.* **132**, 12522–12524 (2010).
52. Men, Y. J. et al. Stomatocyte in stomatocyte: A new shape of polymersome induced via chemical-addition methodology. *Nano Lett.* **18**, 2081–2085 (2018).
53. Li, W. et al. Programmable compartment networks by unraveling the stress-dependent deformation of polymer vesicles. *Small* **20**, 2306219 (2024).
54. Huo, M. & Yuan, J. Y. Polymer assemblies with nanostructure-correlated aggregation-induced emission. *Macromolecules* **50**, 1126–1133 (2017).
55. Zhang, D. P. & Li, M. H. CO₂-Activated reversible transition between polymersomes and micelles with AIE fluorescence. *Angew. Chem. Int. Ed.* **58**, 10260–10265 (2019).
56. Natori, I., Natori, S., Hanawa, N. & Ogino, K. Synthesis of poly(4-diphenylaminostyrene)-poly(1-vinylpyrene) binary block copolymer as a noncovalent cross-linker for single-walled carbon nanotubes (SWNTs) gel: Anionic polymerization of 1-vinylpyrene and formation of self-assembled polymer/SWNTs nanocomposite. *Polymer* **91**, 194–202 (2016).

Acknowledgements

Q.Y. is grateful for the financial support from the National Natural Science Foundation of China (22371053, 21674022, 51703034, 223B2103) and the Outstanding Young Scholar Program.

Author contributions

X.F.L. and Q.Y. conceived the project and designed the experiments and characterizations. Q.Y. supervised and supported the project. X.F.L. and X.L. developed the materials and performed the characterization. X.F.L., C.Q.Y., and Q.Y. analyzed the data. X.F.L. and Q.Y. wrote the paper.

Competing interests

The authors declare no competing interests.

Additional information

Supplementary information The online version contains supplementary material available at <https://doi.org/10.1038/s41467-024-53053-3>.

Correspondence and requests for materials should be addressed to Qiang Yan.

Peer review information *Nature Communications* thanks the anonymous reviewers for their contribution to the peer review of this work. A peer review file is available.

Reprints and permissions information is available at <http://www.nature.com/reprints>

Publisher's note Springer Nature remains neutral with regard to jurisdictional claims in published maps and institutional affiliations.

Open Access This article is licensed under a Creative Commons Attribution-NonCommercial-NoDerivatives 4.0 International License, which permits any non-commercial use, sharing, distribution and reproduction in any medium or format, as long as you give appropriate credit to the original author(s) and the source, provide a link to the Creative Commons licence, and indicate if you modified the licensed material. You do not have permission under this licence to share adapted material derived from this article or parts of it. The images or other third party material in this article are included in the article's Creative Commons licence, unless indicated otherwise in a credit line to the material. If material is not included in the article's Creative Commons licence and your intended use is not permitted by statutory regulation or exceeds the permitted use, you will need to obtain permission directly from the copyright holder. To view a copy of this licence, visit <http://creativecommons.org/licenses/by-nc-nd/4.0/>.

© The Author(s) 2024